Electronic Supplementary Material (ESI) for Sensors & Diagnostics.

Supporting Information

S1: Device Fabrication

Device Fabrication:

The fabrication of the viscometer device involves micromachining a zigzag array of wells in an aluminium (Al) mould with a well depth of H = 1500 μm and a well diameter of D = 300 μm (Figure 1). We chose the microsensor geometry and their arrangement within the microchannel based on the results of CFD studies as shown in Figure S2. To obtain an array of flexible microsensors, PDMS (Sylgard 184, Dow Corning, USA) with a base to curing agent ratio of 10:1 was cast onto the mould and degassed for 30 minutes. Subsequently, the mould was baked at 75 ºC for 60 minutes. Cured PDMS replica was then removed from the mould using a surgical scalpel and two access holes for inlet and outlet were punched. The final device was obtained by treating both the PDMS replica and a glass microscope slide (25×75 mm) in oxygen plasma for 45 seconds and then bringing them into conformal contact. The final device had a height of 1600 μm leaving a gap of 100 μm between the pillar tips and the channel ceiling. The fabrication process explained above is depicted in Figure 1 with panel (d) showing the top image of the final device.[29]

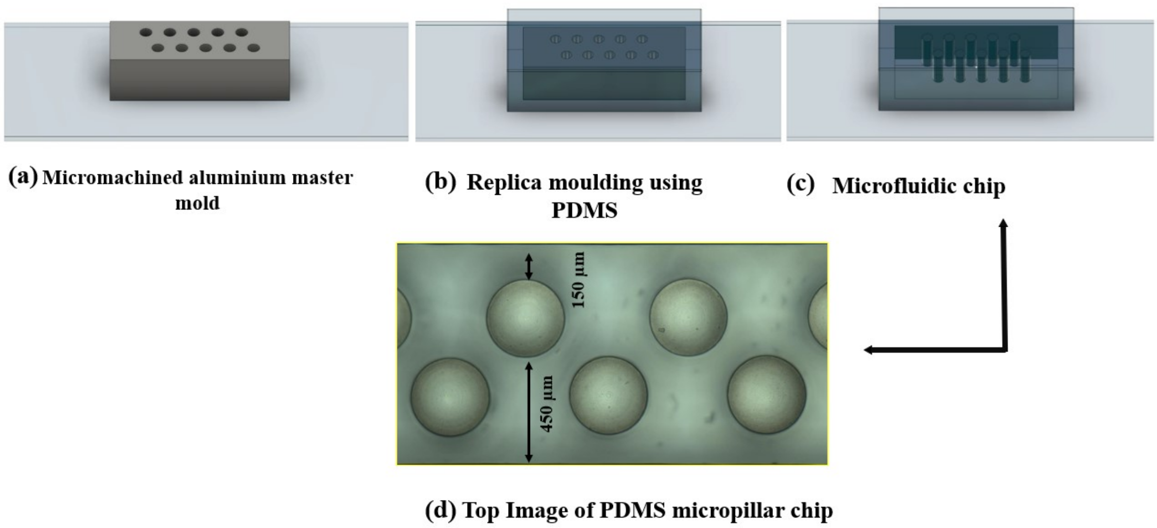

Figure S1 (a) Micromachined aluminium mould having 10 microwells each with an aspect ratio (H:D) of 5:1 (height H = 1500 μm and diameter D = 300 μm). **(b)** PDMS casting and curing at 75 ºC for 60 minutes. **(c)** Final PDMS chip with microsensors of height H = 1500 μm and diameter D = 300 μm. Channel length L = 6000 μm, channel width W = 900 μm. (d) Top image of the fabricated device.

S2: Comparison of CFD and Experimental microsensor deflection data as function of flow rate. (a, b and c). Microsensor deflection data for zigzag and straight microsensor array configurations.

In recent years numerical simulations based on finite element methods have been used to aid the development of microfluidic devices by verifying and optimizing the design and operating parameters. We developed a CFD model for our microfluidic viscometer device based on modelling fluid-structure interactions by coupling laminar form of Navier-Stokes equation to large strain equations for hyperelastic polymers. The governing equations are provided below

$$\rho\left(u_{fluid} \cdot \nabla\right)u_{fluid} = \nabla \cdot [\,-pI + K] + F$$

$$K = \mu\left(\nabla u_{fluid} + \left(\nabla u_{fluid}\right)^T\right) \quad \textbf{(2)}$$

where ρ is fluid density, u is linear velocity, μ is the fluid viscosity, and p is the pressure. The fluid was modelled as an incompressible fluid by coupling Equation 1 with the continuity equation:

$$\rho\nabla \cdot u_{fluid} = 0 \quad \textbf{(3)}$$

Equations of motion for large strains were solved to account for deflection of PDMS microsensors under shear stress.

$$0 = \nabla \cdot (F \cdot S)^T + Fv \quad \textbf{(4)}$$

The CFD model assumed that the microsensor base is fixed, that is $\mu_{solid} = 0$, which ensures that deflection due to shear stress is maximum at the pillar tip and zero at the pillar base. COMSOL Multiphysics module was used to solve for the coupled equations listed above and obtain the microsensor tip deflection values for each fluid sample at a given flow rate. A user-controlled mesh was created with a maximum element size of 1330 μm and a minimum element size of 180 μm. Entire geometry was calibrated for fluid dynamic physics using free tetrahedral sub node, effectively creating an unstructured mesh. Boundary layer properties were adjusted by choosing a boundary layer stretching factor of

1.2 and a thickness adjustment factor of 5. We assumed that field variables do not change over time hence, stationary study node was used for computing results. In order to The CFD studies were performed for two different viscometer geometries (zigzag and straight). Figure S1 a, b and c compares the CFD simulation results with our experimental results while in Figures S1 d, e and f we compare two microfluidic geometries zigzag and straight.

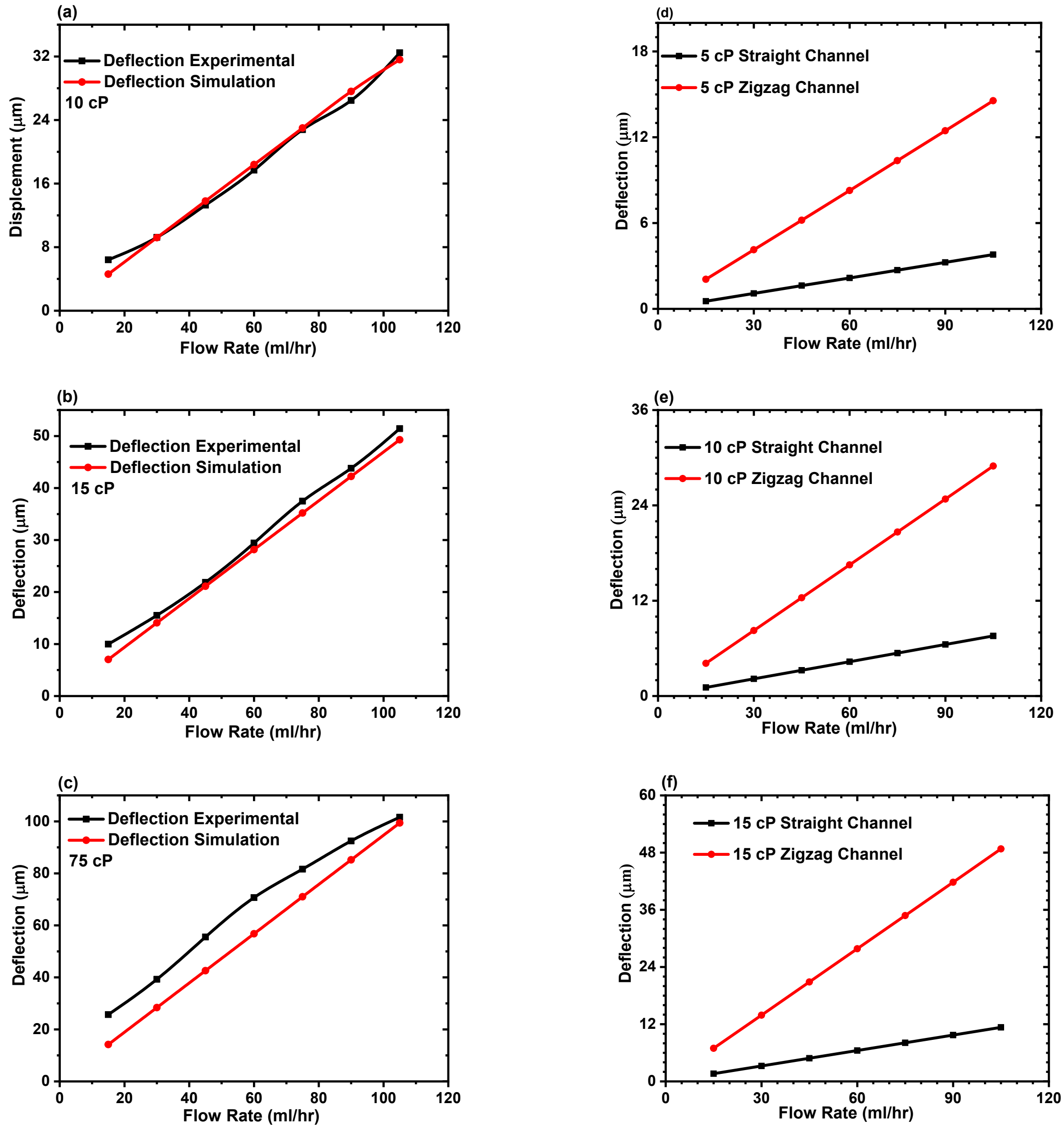

Figure S2. Comparison between experimental and CFD simulation results for (a) 10 cP, (b) 15 cP and (c) 75 cP. Flow rate versus tip deflection for (d) 5 cP, (e) 10 cP, and (f) 15 cP solutions in microchannels with zigzag and straight microsensor arrangement.

The results in Figure S2 d, e and f depict that the microfluidic viscometer with a zigzag microsensor arrangement yields higher tip deflection compared to a straight microsensor arrangement due to enhanced fluid-structure interaction [29, 31, main text].

S3: Variation in Deflection Amplitude from Pillar to Pillar

Through CFD simulations, we concluded that microsensors in the middle of the array were more responsive to the changes in flow rate and viscosity. We observed that microsensor #6 displayed the highest deflection values compared to other pillars in the array. For instance, results shown in Figure S2 depict that at a flow rate of 45 ml/hr microsensor #1 yields a deflection of 4 µm whereas microsensor #6 yields a deflection of 6 µm. Based on these results, we decided to use tip deflection of microsensor #6 to obtain viscosity values.

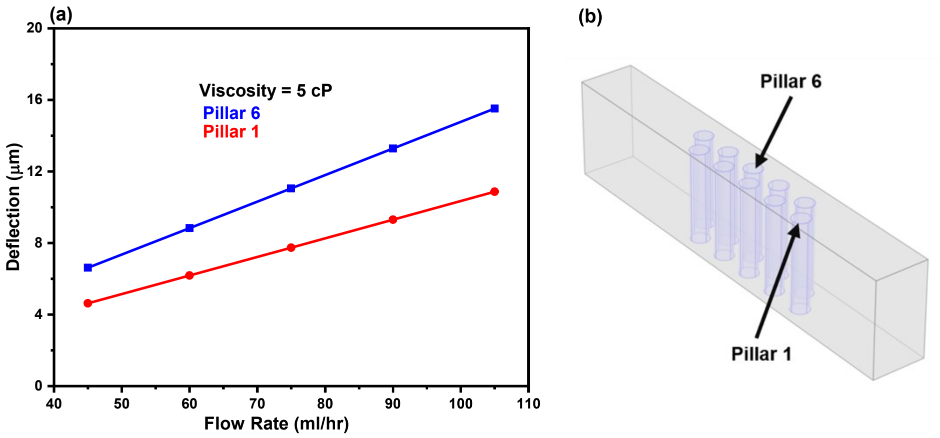

Figure S3. (a) Flow rate versus deflection plots for pillar #1 and pillar #6 for a 5 cP solution. (b) Pillar arrangement in microchannel.

S4: Comparison of different CFD models of Viscosity vs Flow rate (Blood sample)

To determine microsensor deflection, we adopted a method similar to the Newtonian fluid case, primarily coupling laminar flow with solid mechanics; however, this time by choosing inelastic non-Newtonian constitutive relation for the infused fluid. The parameters for both models were chosen from literature [40–42]. The results shown in Figure S4.1 compare the blood viscosity values measured using our microsensor-based viscometer with those calculated using power law and Carreu model. At 15ml/hr, the viscosity of blood is measured to be 5.4 cP and when the flow rate is increased to 105ml/hr, the viscosity reduces to 2.7 cP due to shear thinning. Similarly, Carreu model for non-Newtonian fluids predicts the blood viscosity to be 4.6 cP at 15ml/hr and 1.7 cP at 105 ml/hr. The results indicate that power law for non-Newtonian fluids more accurately models the shear-thinning behaviour of blood for our microfluidic viscometer. A shear rate versus viscosity plot was also generated for the whole blood sample as shown in Figure S4.3. The results indicated a decrease in the whole blood viscosity with increasing shear rate.

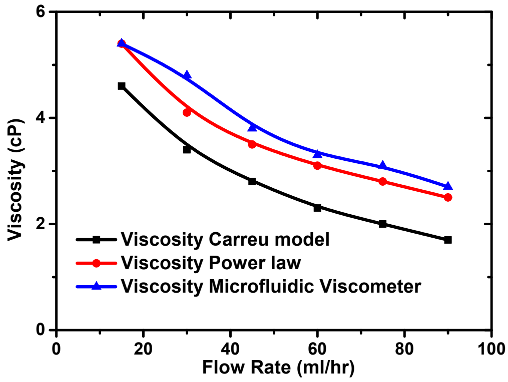

Figure S4.1 Comparison of experimental and CFD-based measurements of viscosity of whole blood samples using a microfluidic viscometer and CFD simulations based on power law and Carreau models.

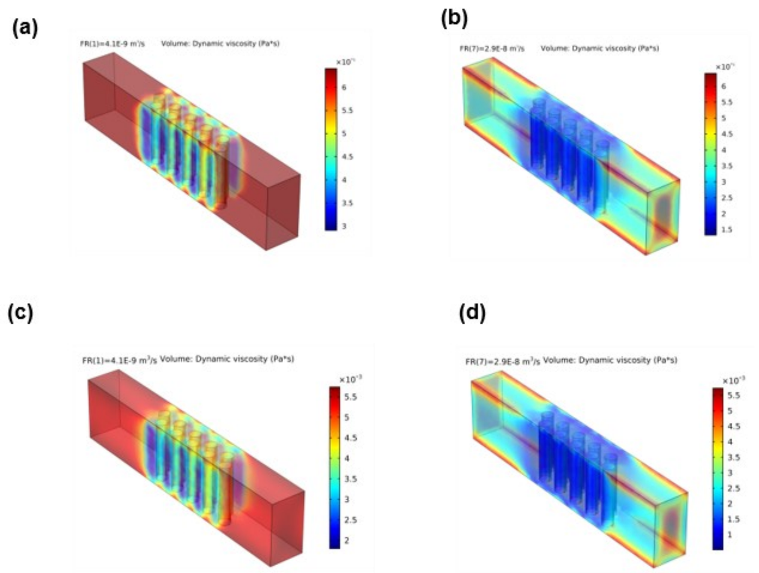

Figure S4.2 (a) Power law viscosity measurement at 15ml/hr. (b) Power law viscosity measurement at 105ml/hr. (c) Carreau model viscosity measurement at 15ml/hr. (d) Carreau model viscosity measurement at 105ml/hr.

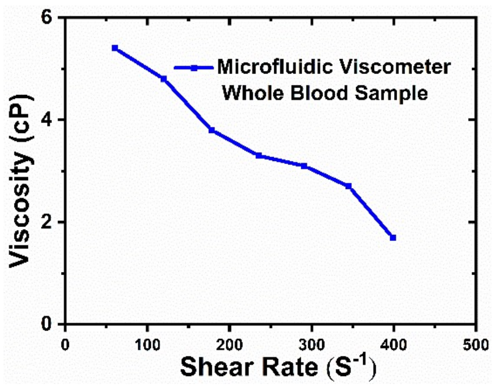

Figure S4.3. Viscosity (cP) versus shear rate (s^{-1}) plot for whole blood sample. The blood sample exhibits shear-thinning behaviour, characterized by a decrease in viscosity with increasing shear rate.

S5: Effect of Aspect Ratio on Microsensor Deflection

Microsensors with higher aspect ratios yield larger deflections under the same flow rate and viscosity. The sensitivity of the microfluidic viscometer therefore increases with higher aspect ratio microsensors; however, this also results in reduction of the dynamic range of the device. We verified this increase in sensitivity and decrease in dynamic range through CFD analysis of microsensors with an aspect ratio of 5:1 (H = 1500 µm : D = 300 µm) and 10:1 (H = 3000 µm : D = 300 µm) as shown in Figure S4. While microsensors with higher aspect ratio are more sensitive, fabrication process of these microsensors poses additional challen

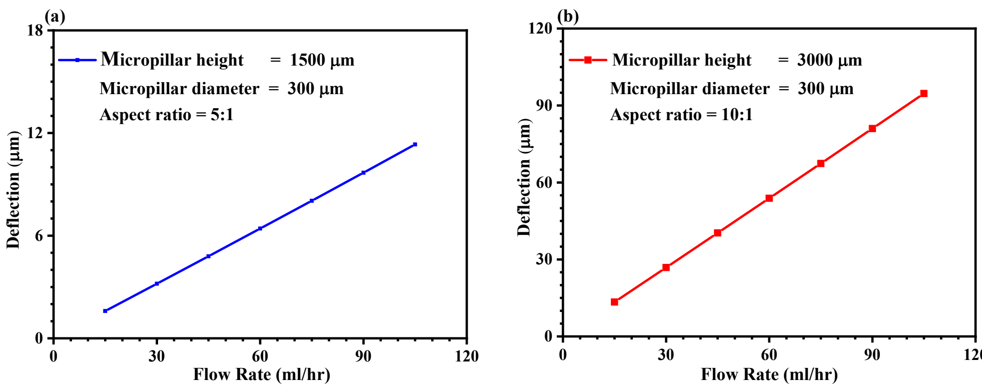

ges.

Figure S5. Comparison of microsensor tip deflection with different aspect ratios. Flow rate versus microsensor tip deflection for (a) 5:1 (b) 10:1 aspect ratio microsensors.

S6: Machine Learning Concepts

Classification of the data is an important step during this work. Using machine learning (ML) algorithms helped us to prove the feasibility of the device. During the process we tested the device accuracy by using two ML algorithms, i.e., Support Vector Machine (SVM) and K-Nearest Neighbour (k-NN). k-NN showed better performance as compared to SVM.

Data representation and its classification is the key factor for any system to be validated. ML is the concept of representing the data in its compressed form. As per saying "Machine learning (ML) is the field of study that gives computer the ability to learn without being explicitly programmed. ML is categorised into two types, known as supervised and unsupervised learning. Both SVM and k-NN represents the supervised learning.

Results:

We used 1323 data samples where 926 data samples (70% of total data) were used for training and 397 data samples for validation. The training accuracy and validation accuracy of all data using ML algorithms are presented in Table 1. In SVM, support vectors play an essential role as they are the points that lie closest to the supporting hyperplane. While training SVM, 610 out of a total of 926 data samples were utilized as support vectors. In Table 2, we presented the number of supporting vectors used for each class.

From Table 1, it is clearly visible that both algorithms are providing acceptable accuracy results, where the result of k-NN higher than SVM. The classification result is commonly depicted in the confusion matrix. The confusion matrix always helps to figure out how the accuracy result appears and miss prediction between classes. The confusion matrix of SVM and k-NN is presented in Tables 2 and 3.

Table 1: List of support vectors in SVM

Support Vectors in SVM		
Class	Number of Support Vectors	Total
5 cP	80	610
10 cP	88	
15 cP	95	
25 cP	80	
50 cP	95	
75 cP	87	
100 cP	85	

Table 2: Confusion matrix of SVM with known viscosities.

SVM Confusion Matrix with 397 Samples								
		Predicted						
	Class	5cP	10 cP	15 cP	25 cP	50 cP	75 cP	100 cP
Actual	5 cP	**55**	1	0	0	0	0	0
	10 cP	9	**49**	0	0	0	0	0
	15 cP	5	1	**48**	2	0	0	0
	25 cP	0	0	0	**57**	0	0	0
	50 cP	0	0	0	0	**47**	9	0
	75 cP	0	0	0	4	0	**49**	3
	100 cP	0	0	0	0	5	2	**51**

Table 3: Confusion matrix of k-NN with known viscosities.

k-NN Confusion Matrix with 397 Samples								
		Predicted						
	Class	5cP	10 cP	15 cP	25 cP	50 cP	75 cP	100 cP
Actual	5 cP	**55**	1	0	0	0	0	0
	10 cP	2	**56**	0	0	0	0	0
	15 cP	5	1	**56**	2	0	0	0

	25 cP	0	0	0	**58**	0	0	0
	50 cP	0	0	0	0	**55**	1	0
	75 cP	0	0	0	4	0	**55**	3
	100 cP	0	0	0	0	5	2	**56**

From Table 3, we can observe that, from class 5cp, only 1 data mismatched with other class 10 cP, and from the class 25 cP, no data mismatched with other classes. Data from the rest of the five classes are mismatched with other classes, and the mismatched ratio stays between 2 and 9.

From Table 4, we can see that, from class 5 cP and 50 cP, only 1 data mismatched with other class. All the data from class 25 cP predicted successfully, so there is no mismatch with other classes. Data from the rest of the four classes are mismatched with other classes, and the mismatched ratio stays between 2 and 8.

We employed three important matrices to evaluate the performance of the used ML algorithms. Employed matrices are precision (PR), recall (RE), and f1-score (F1), and they can be defined as,

Precision helps to measure how many data points are correctly predicted by the model over the amount of correct and incorrect predictions. Recall is used to measure how many data points are correctly predicted by the model over the total amount of data points. F1-score measures the overall accuracy of a model by combining precision and recall. An excellent F1-score stands for low false positives and low false negatives, which correctly identifies real threats. F1-score is always considered as perfect when it has value 1. On the other hand, the model is considered as bad when it has 0. Table 5 presented precision, recall, and F1-score of SVM and k-NN algorithm accordingly.

Table 4: Calculated performance matrices of SVM.

SVM Performance Result (%)			
Class	**Precision**	**Recall**	**F1-Score**
5 cP	0.79	0.98	0.88
10 cP	0.96	0.84	0.89
15 cP	1	0.85	0.92
25 cP	0.90	1	0.95

50 cP	0.90	0.83	0.87
75 cP	0.81	0.87	0.84
100 cP	0.94	0.88	0.91

Table 5: Calculated performance matrices of k-NN.

k-NN Performance Result (%)			
Class	**Precision**	**Recall**	**F1-Score**
5 cP	0.96	0.98	0.97
10 cP	0.98	0.96	0.97
15 cP	1	1	1
25 cP	1	1	1
50 cP	1	0.98	0.99
75 cP	0.94	1	0.97
100 cP	1	0.96	0.98

Table 5 shows a higher value of the f1-score achieved when both precision and recall values are high, which means the mismatched ratio between each class is low. Between SVM and k-NN, k-NN achieved higher f1-scores than SVM.

S7: Experimental Videos

ESI. (a) Aqueous Glycerol 50 cP, 15 ml/hr.

Movie depicts microsensor deflection as the fluid (Aqueous glycerol with a viscosity of 50 cP) is infused into the microfluidic viscometer at 15ml/hr. The microsensors deflect as the fluid passes through the device and eventually come back to their original position once the flow is stopped.

ESI. (b) Whole blood sample 5.74 cP, 45 ml/hr

Movie depicts microsensor deflection as the whole blood(Viscosity value of 5.74 cP) is infused into the microfluidic viscometer at 45ml/hr. The microsensors deflect as the blood passes through the device and eventually come back to their original position once the flow is stopped.

ESI. (c) Whole blood coagulation at 15 ml/hr

The movie depicts the coagulation of whole blood sample. We can see that as blood coagulates its viscosity increases. This increase in viscosity is translated into an apparent increase in the deflection of the microsensor.